Received: 13 September 2019 | Revised: 23 March 2020 | Accepted: 24 March 2020

DOI: 10.1002/mrm.28284

FULL PAPER

Magnetic Resonance in Medicine

Efficient ^{23}Na triple-quantum signal imaging on clinical scanners: Cartesian imaging of single and triple-quantum ^{23}Na (CRISTINA)

Michaela A. U. Hoesl[1] | **Lothar R. Schad**[1] | **Stanislas Rapacchi**[2]

[1]Computer Assisted Clinical Medicine, Heidelberg University, Mannheim, Germany

[2]Aix-Marseille University, CNRS, CRMBM, Marseille, France

Correspondence
Michaela A. U. Hoesl, Computer Assisted Clinical Medicine, Heidelberg University, Mannheim 68167, Germany.
Email: michaela.hoesl@gmail.de

Funding information
European Cooperation in Science and Technology, Grant/Award Number: STSM Action: "CA16103 Assessment of Kidney Physi; France Life Imaging network, Grant/Award Number: grant ANR-11-INBS-0006; Investissements d'Avenir programme, Grant/Award Number: grant ANR-11-EQPX-0001; laboratory member of France Life Imaging network, Grant/Award Number: ANR-11-INBS-0006; platform 7 T-AMI, a French "Investissements d'Avenir" programme", Grant/Award Number: ANR-11-EQPX-0001

Purpose: To capture the multiquantum coherence (MQC) ^{23}Na signal. Different phase-cycling options and sequences are compared in a unified theoretical layout, and a novel sequence is developed.

Methods: An open source simulation overview is provided with graphical explanations to facilitate MQC understanding and access to techniques. Biases such as B_0 inhomogeneity and stimulated echo signal were simulated for 4 different phase-cycling options previously described. Considerations for efficiency and accuracy lead to the implementation of a 2D Cartesian single and triple quantum imaging of sodium (CRISTINA) sequence employing two 6-step cycles in combination with a multi-echo readout. CRISTINA was compared to simultaneous single-quantum and triple-quantum-filtered MRI of sodium (SISTINA) under strong static magnetic gradient. CRISTINA capabilities were assessed on 8 × 60 mL, 0% to 5% agarose phantom with 50 to 154 mM ^{23}Na concentration at 7 T. CRISTINA was demonstrated subsequently in vivo in the brain.

Results: Simulation of B_0 inhomogeneity showed severe signal dropout, which can lead to erroneous MQC measurement. Stimulated echo signal was highest at the time of triple-quantum coherences signal maximum. However, stimulated echo signal is separated by Fourier Transform as an offset and did not interfere with MQC signals. The multi-echo readout enabled capturing both single-quantum coherences and triple-quantum coherences signal evolution at once. Signal combination of 2 phase-cycles with a corresponding B_0 map was found to recover the signal optimally. Experimental results confirm and complement the simulations.

Conclusion: Considerations for efficient MQC measurements, most importantly avoiding B_0 signal loss, led to the design of CRISTINA. CRISTINA captures triple-quantum coherences and single-quantum coherences signal evolution to provide complete sodium signal characterization including T_2^* fast, T_2^* slow, MQC amplitudes, and sodium concentration.

KEYWORDS
^{23}Na MRI, coherence transfer, multiple-quantum coherences, triple-quantum sodium imaging

Lothar R. Schad and Stanislas Rapacchi contributed equally to this work.

1 | INTRODUCTION

Multiquantum sodium (^{23}Na) NMR was first been investigated and described 3 decades ago.[1–5] Recently, technological advances have led to a revival of ^{23}Na MRI, with a particular interest in the potential to link multiquantum ^{23}Na MRI to underlying pathophysiological pathways.[6–9] In standard ^{23}Na imaging experiments, detection of the single-quantum (SQ) transition is performed directly after an excitation with similar approaches to conventional proton MRI. To exploit the potential of the spin 3/2 nuclei, multiquantum coherence (MQC) signals are built by coherence transfer and combined over multiple acquisitions using RF phase cycling. Eventually, ^{23}Na triple-quantum coherences (TQC) might provide additional information related to cell vitality compared to the single-quantum coherences (SQC) signal alone.[10] A clear understanding of the mechanisms of MQC is necessary for relevant measurements and evading potential pitfalls. The description of MQC can be found in the clean form of the tensor formalism but spread in several papers[1,5,11–14] dating of 15 years at the least. These highly theoretical descriptions neither offer an intuitive way of understanding multiquantum mechanisms in the multidisciplinary field of MRI nor provide a basis to easily describe and relate the recent advances in triple-quantum (TQ) ^{23}Na NMR and MRI.

^{23}Na spin 3/2 nuclei exhibit 4 possible energy levels. Depending on the surrounding medium, different transitions between the levels are possible. The electric quadrupole interaction determines the ^{23}Na relaxation processes and fundamentally distinguishes it from the dominant dipole–dipole interaction of proton nuclei. Due to the quadrupolar nature of the sodium nuclei, higher quantum coherences can be measured when the correlation time (describing the fluctuations of the electric field gradient at the ^{23}Na nuclei)[15] exceeds the Larmor period. The electric field gradient is generated by the electrons of the surrounding environment (ie, proteins, lipids, macromolecules). In biologic environment, there is a fluctuating quadrupolar interaction, which adds to the Zeeman splitting and leads to a biexponential relaxation behavior so that MQC signals in the form of double quantum coherence (DQC) and TQC can be observed (Figure 1A). ^{23}Na MQC signal gives information about the interaction of the ^{23}Na nuclei with its surrounding environment in vivo.

In an anisotropic environment, the quadrupolar moment of the ^{23}Na nuclei couples to the electric field gradient, which acts as relaxation mechanism leading to a more rapid decay of the outer than inner transitions of the spin 3/2 energy levels, resulting in a biexponential T_2 relaxation with fast and slow components, which gives the possibility of MQC transfer due to violation of the coherence transfer rules.[1,4,16] In contrast, the quadrupole moment does not couple to an isotropic field; therefore, no MQC can be measured in isotropic medium (eg, saline solution).

A static quadrupolar interaction is observed in further macroscopically ordered environments, which is rare in biological medium but can be found in cartilage. DQC signal can yield information about the anisotropy in tissue because in ordered structures a preferred orientation of the quadrupolar ^{23}Na nuclei relative to the magnetic field B_0 exists. DQC arise from 2 mechanisms: biexponential relaxation (T_{32}) and quadrupolar splitting (T_{22}); for specific information about the anisotropy, a magic angle sequence selects the signal arising from T_{22}.[4,17,18] In contrast, TQC signal arises only due to biexponential relaxation. Quadrupolar splitting within anisotropic structures has no additional effect.[11,12] Figure 1 shows the relevant processes.[16]

To measure and filter for different coherence pathways, in general, a 3-pulse sequence is needed along with RF phase cycling to select the coherence of interest.[2] In this paper, we want to give an intuitive and pictorial understanding of phase cycling-based MQC buildup and the available choices in the corresponding 3-pulse experiment. The purpose was to seek optimal efficiency of a 3-pulse sequence, defined in this scope as the minimum number of cycles and steps per cycle to provide a complete and unbiased measurement of MQC ^{23}Na signals. Thus, a time-efficient sequence design is drawn from analytical and simulation results. This sequence is guaranteed to withstand B_0 and stimulated echo (STE) biases and is optimal for clinical MQC imaging methods. Experimental results demonstrate the potential of proposed Cartesian imaging of single and triple-quantum ^{23}Na (CRISTINA).

2 | THEORY

The pulse sequence is depicted along with the coherence pathway scheme in Figure 1. The conventional 3-pulse experiment introduces 3 time constants as parameters that impact the eventual measured signal. Among these 3, τ_2 is usually minimized to neglect relaxation between the second and the third pulse; however, the evolution time, τ_1, and the TE are in strong relation with the biexponential relaxation that separates SQC from DQC and TQC. The sequence is repeated while cycling the phases of the RF pulses. The first pulse phase, ϕ_1, cycles through a defined phase cycle, whereas the second pulse is phase-shifted by the "phaseshift, ξ" relative to the first pulse. The second pulse phase ϕ_2 will be given in relation to the first throughout the paper by its phase shift $\xi = \phi_2\text{-}\phi_1$. The phase of the third pulse is set to 0°, as is the receiver phase. Exploiting the differences in evolution frequency between the MQC signals, an addition of the signals, leads to constructive and destructive interference of the MQC pathways depending on the selected phase cycling scheme. The multiple aspects of MQC measurements are covered in the following.

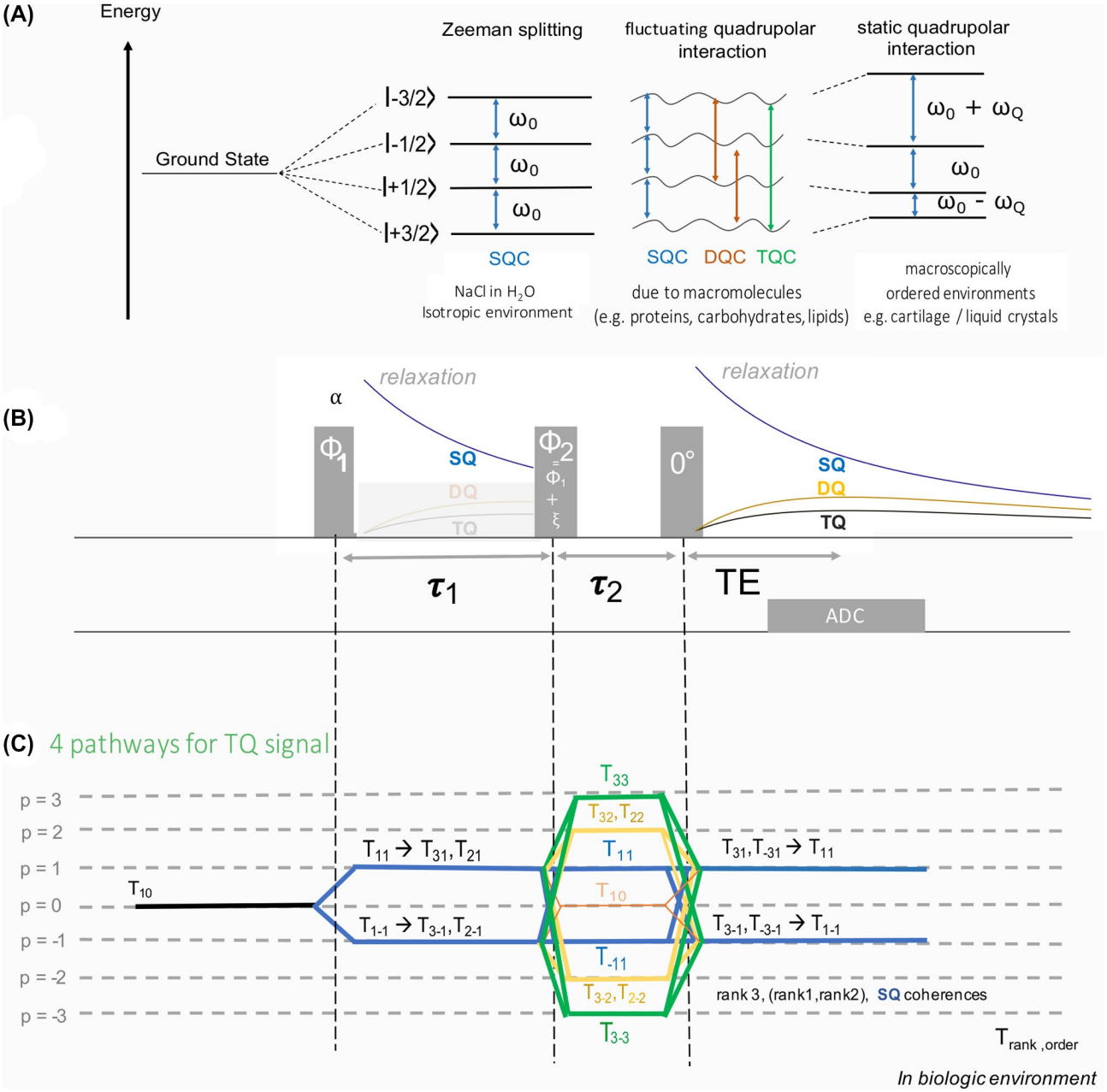

FIGURE 1 A, ^{23}Na spin 3/2 nuclei interaction with a magnetic field. In isotropic environment, the ground state splits into the 4 different energy levels with equidistant levels. In biologic environment, fluctuating quadrupolar interaction leads to the observation of DQC and TQC. Static quadrupolar interaction in ordered environments is rare in biological medium. B, The three pulses experiment used to achieve MQC transfer C, coherence transfer diagram for pathways that can be probed. Relaxation between the first and second pulse, τ_1, is crucial for TQC creation. The time between the second and third pulse (τ_2) is chosen as short as possible to limit MQC signal loss. The tensor $T_{rank,order}$ changes its order after each RF pulse, whereas only relaxation and quadrupolar coupling change the rank of the tensor. In perfect quadrature detection, only coherence level of −1 is observable. However, imperfect quadrature detection is common in MRI, and signals can end up in the +1 pathway as well. ^{23}Na, sodium; DQC, double quantum coherence; MQC, multiquantum coherence; TQC, triple-quantum coherences

Different phase cycling options have been proposed to eliminate potential biases in MQC measurements. Four options have been highlighted, which are presented in summary in Table 1.

First, the original 6 steps phase cycle, option I, which samples the coherence evolution over a 2π interval with a phase increment of π/3, a phase shift $\xi = \pi/2$, $\phi_{1,t=0} = \pi/6$, and a constant phase for the third pulse and the receiver of 0°.[1] The phase increment of π/3 places the TQ frequency at the Nyquist limit.

Second, option II, the 2 × 8-steps NMR method of triple-quantum (time) proportional phase increments TQ(T)PPI.

TABLE 1 Overview over the highlighted phase-cycle options

	Phase cycles	$\Delta\phi_1$		$\phi_{1,t=0}$	$\xi = (\phi_2\text{-}\phi_1)$	Acronym
Option I	1 × 6 steps	π/3	One cycle	π/6	π/2	Original[1]
Option II	2 × 8 steps	π/4	First cycle	π/2	π/2	TQ(T)PPI[19,20]
			Second cycle	π/2	−π/2	
Option III	2 × 6 steps	π/3	First cycle	π/2	π/2	Fleysher[26]
			Second cycle	0	0	
Option IV	4 × 6 steps	π/3	In vivo cycles	π/6	π/2	SISTINA[22]
				7π/6	−π/2	
			Phantom cycles	2π/3	0	
				5π/3	0	
Option V	2 × 6 steps	π/6	First cycle	π/2	π/2	CRISTINA
			Second cycle	0	0	

Abbreviations: CRISTINA, Cartesian imaging of single and triple-quantum ^{23}Na; SISTINA, simultaneous single-quantum and triple-quantum-filtered MRI of ^{23}Na; TQ(T)PPI, triple-quantum (time) proportional phase increments.

This NMR method was developed to circumvent the need to optimize τ_1 and TE, and focus on capturing the relaxation constants T_2^* slow and T_2^* fast by incrementing τ_1.[19] This sequence was employed for ^{23}Na TQC measurement with an 8-step phase cycling, proposed to measure directly the T_2 relaxation.[20] Its advantage is a signal acquisition free of assumptions on the sample(s) relaxation parameters. The TQ(T)PPI with optional increments of the evolution time was used by Refs. 1, 20 with a phase shift of $= +\pi/2$. An additional 8-step phase cycle with $= -\pi/2$ was proposed to eliminate DQC with $\phi_1^{\text{1st\_cycle}} = \phi_1^{\text{2nd\_cycle}}$.

Third, option III, a 2 × 6-steps cycle for recovering signal cancellation due to deleterious effects of B_0 inhomogeneity, was proposed by Fleysher et al.[21] In MRI, B_0 inhomogeneity can be severe and lead to spins dephasing and MQC signal loss. An additional 6-step phase cycle was introduced with phase shift = 0 (Table 1). Gradient spoiling during evolution time would be an alternative to mitigate B_0 inhomogeneity impact but lowers the SNR due to the spoiling of half the coherence pathway contributions.

Fourth, option IV uses 4 × 6 steps phase cycling to avoid bias due to T_1-weighted STE signals, presented by Fiege et al.[22] Signal bias can arise due to STE signal for which a solution, the SISTINA sequence, was proposed by Tanase and Boada[13] and Fiege et al.[22] In general, a 3-pulse sequence can form a STE signal[23–25] that could give an unwanted bias. An additional phase cycle was introduced with a phase shift of $= -\pi/2$. SISTINA chose two 6-steps phase cycles, with phase shifts $= \pm\pi/2$, to eliminate STE signal. B_0 inhomogeneity was compensated for with 2 extra phase cycles, for a total of 4 phase cycles, using the same approach as in option III.

In the following, the impact of STE versus B_0 offset was investigated to make a founded choice, our option V, for optimal MQC measurement.

3 | METHODS

3.1 | Simulation

For the formulation of the signal equations, Fleysher et al[21] formalism was chosen, and detailed description can be found (https://github.com/MHoesl/MQC_Simulation). The coherence levels after the first and second RF pulses are denoted by $p1$ and $p2$, respectively. The matrix $A_{p1,p2}$ was specified as the amplitude of the respective coherence pathway:

$$A_{p1,p2} = \begin{array}{c|ccccccc} \frac{p2\rightarrow}{p1} & -3 & -2 & -1 & +1 & +2 & +3 \\ -1 & -\text{TQ}/4 & -\text{DQ}/4 & -\text{SQ}/4 & -\text{SQ}/4 & -\text{DQ}/4 & -\text{TQ}/4 \\ +1 & \text{TQ}/4 & \text{DQ}/4 & \text{SQ}/4 & \text{SQ}/4 & \text{DQ}/4 & \text{TQ}/4 \end{array}$$

An initial amplitude set (SQ, DQ, TQ) for the coherence level transfers is thus divided into its multiple possible pathways. For example, there are 4 possibilities for the TQC (drawn in green in Figure 1C). One of these 4 pathways starts from the coherence level $p1 = -1$ after the first pulse. The second pulse transfers to the coherence level to $p2 = -3$, resulting in the signal from $T_{3\text{-}3}$. The received signal, S, cumulates all coherence pathways and is expressed as:

$$S\left(\tau_1, \tau_2, \phi_1, \phi_2, \Omega, \text{TE}\right) = \sum_{p1}\sum_{p2} e^{-i\left(p_1\phi_1+(p_2-p_1)\phi_2\right)} B_{\text{Na}}\left(p_1, p_2, \tau_1, \tau_2, \Omega, \text{TE}, A_{p1,p2}\right) \quad (1)$$

$$B_{\text{Na}} = e^{-i\left(p_1\tau_1+p_2\tau_2\right)\Omega} e^{i\Omega TE} A_{p1,p2}.$$

The parameter Ω (Hz) in the term B_{Na} describes the off-resonances effects for simulation of magnetic field inhomogeneity. Theoretically, the signal S is nulled for:

$$S(\Omega)=0 \quad \text{for} \quad \Omega\,(\text{Hz})=\frac{k\pi+\xi}{2\pi\tau_1},\ k\in\mathbb{Z}.$$

Details can be found in Supporting Information Calculation S1.[26] For the first simulation part, relaxation terms were omitted. For the second simulation part, the following equations were formulated to take into account relaxation effects within the amplitude matrix $A_{p1,p2}$. SQ signal was described by the biexponential decay separated into T_2^* slow and T_2^* fast components and the excitation angle θ_{exc}:

$$SQ=SQ_0\left(\frac{3}{5}e^{-\frac{(TE+\tau_1)}{T2^*_{slow}}}+\frac{2}{5}e^{-\frac{(TE+\tau_1)}{T2^*_{fast}}}\right)\sin\left(\theta_{exc}\right). \quad (2)$$

For the DQ and TQ coherence signals, the relaxation terms are given by:

$$MQ = MQ_0\left(e^{-\frac{TE}{T2^*_{slow}}}-e^{-\frac{TE}{T2^*_{fast}}}\right)\left(e^{-\frac{\tau_1}{T2^*_{slow}}}-e^{-\frac{\tau_1}{T2^*_{fast}}}\right)e^{-\frac{\tau_2}{T2^*_{slow}}}\sin^5\left(\theta_{exc}\right),\ \text{with MQ = DQ, TQ} \quad (3)$$

The STE signal depends on the flip angle (or B1+), relaxation effects, and B_0 inhomogeneity, and was described as follows:

$$S_{STE}=\sum_{p1}\sum_{p2}e^{-i\left(p_1(m)\phi_1+(0-p_1(m))\phi_2\right)}B_{STE}\left(\tau_1,\ \tau_2,\ \Omega,\ TE,\ \xi,\ T_1,\ T2^*_{slow},\ T2^*_{fast},\ A_{p1,p2}\right) \quad (4)$$

$$B_{STE}=\frac{\left|A_{p1,p2}\right|}{2}e^{-\frac{\tau_2}{T_1}}\cos\left(\xi-\Omega\tau_1\right)e^{i\Omega TE}\left(\frac{3}{5}e^{-\frac{(TE-\tau_1)^2}{2T2^{*2}_{slow}}}+\frac{2}{5}e^{-\frac{(TE-\tau_1)^2}{2T2^{*2}_{fast}}}\right). \quad (5)$$

The maximum of B_{STE}, with respect to the TE, is found for $TE=\tau_1$. We used the following parameter values in accordance with realistic measurement values: τ_1 = 10 ms, τ_2 = 100 µs, T_2^* slow = 30 ms, T_2^* fast = 4 ms, and T_1 = 70 ms. All 3 flip angles were set to π/2. The MQC signal contributions, which populate the matrix $A_{p1,p2}$, were set to 1.0, 0.5, and 0.3 for the SQ, DQ, and TQ coherences, respectively, to ease visualization. Assuming sufficiently long TR values (> 120 ms), notably to fit practical SAR limitations in MRI, T_1 relaxation was further neglected in the simulations.

SIGNAL RECONSTRUCTION: MQC signals can be separated by their scaled evolution frequencies, as defined by their phase term $\exp\left(-i\left(p_1\phi_1+\left(p_2-p_1\right)\phi_2\right)\right)=\exp(-ip_2\phi_1)\exp\left(i(p_2-p_1)\xi\right)$. The spectrum signal is thus reconstructed by Fourier transformation along the phase dimension ϕ_1. According to Fleysher, the signals, S, of the 2 phase-cycles, are transformed independently:

$$\hat{S}_{\{\xi\}}=\text{FT}(S_{\{\xi\}}),\ \ \xi=\frac{\pi}{2},\ 0. \quad (6)$$

$\hat{S}$ denotes the spectrum, normalized to the size of the signal to obtain correct Fourier transformation amplitude values. The 2 spectra are combined to $\hat{S}_{\pm}$.

$$\hat{S}_{\pm}=\frac{1}{2}\left(\hat{S}_{\{\xi=0\}}\pm i\hat{S}_{\left\{\xi=\frac{\pi}{2}\right\}}\right). \quad (7)$$

A fully recovered spectrum, $\hat{S}$, can be calculated if the B_0 offset, $\boldsymbol{\Omega}$, is known. Signal dephasing occurs during the evolution time and the TE, and the signal can be recovered with its phase:

$$\hat{S}_{reco}\Big|_{t=TE,B0offset=\Omega}=\frac{1}{2}\left(\hat{S}_+\Big|_{TE,\Omega}e^{+i\Omega\tau1}-\hat{S}_-\Big|_{TE,\Omega}e^{-i\Omega\tau1}\right)e^{-i\Omega TE}. \quad (8)$$

For the SISTINA reconstruction, in total 4 cycle-signals (4 × 6 steps) were proposed to offer a full reconstruction correcting for STE signal and B_0 offset. But in vivo SISTINA acquisitions were limited to phase cycles 1 and 2 only. Thus, the reconstruction was reported as individual signal Fourier transformation and sum-of-squares combination:

$$\hat{S}_{\{n\}}=FT\left(S_{\{n\}}\right),\ n=1,2,3,4,\ \hat{S}\Big|_{\text{invivo}}=\sqrt{\hat{S}_1^2+\hat{S}_2^2} \quad (9)$$

$$\hat{S}\Big|_{\text{total}}=\sqrt{\hat{S}_1^2+\hat{S}_3^2+\hat{S}_2^2+\hat{S}_4^2}. \quad (10)$$

The signals, S, and resulting spectra, $\hat{S}$, were simulated for 1) the original 6-step phase cycle as well as the highlighted options, 2) 2 × 8-step TQ(T)PPI phase cycle, 3) the 2 × 6 step phase cycles of Fleysher, and 4) the 4 × 6 phase cycles of the SISTINA sequence.

3.2 | Experimental acquisitions

To complement the simulation work, measurements on 2 phantoms and in the brain of 5 healthy volunteers were performed. Experiments were performed on 7 T MRI (Siemens Magnetom, Erlangen, Germany) with a 1Tx/1Rx dual-tuned ^{1}H/^{23}Na head coil (QED, Cleveland, OH). One phantom was a simple bottle of saline water. The second phantom consisted of 8 × 60 mL tubes, with varying concentrations of agarose

(0%-5%) and ^{23}Na (50-154 mM). The study was approved by local ethical committee, and volunteers were recruited after providing informed consent according to the Declaration of Helsinki. Three vials were placed next to the head, with concentrations of agarose and ^{23}Na of: (4% 100 mM), (% 50 mM), and (2% 100 mM) to allow subsequent calculations of tissue sodium content and comparison of TQ signal. A multi-echo Cartesian MQC imaging sequence was developed that features the possibility of easy switching between different phase cycle choices by variable Φ_0, $\Delta\Phi$, and phase shift ξ. A Cartesian readout was chosen for efficiency and ease of reconstruction, as well as because the TQC signal of interest is maximal at a later TE (Figure 1B). Efficiency considerations included the number of measured points per phase cycle and the use of a multi-echo readout, which allows signal capture of both TQC (later TEs) and SQC (early TEs), as well as the possibility of reconstructing a B_0 map directly from the data. $\Delta\Phi$was conservatively chosen to be 30°, which results in a twofold oversampling of the TQC frequency. The 12-steps phase cycle of 2π was averaged over 10 repetitions in phantom and 12 repetitions in vivo. Other parameters were: 32×32 matrix size with twofold oversampling in readout direction, FOV of 200 mm (phantom) and 250 mm (in vivo), bandwidth of 330 Hz/Px, and 2D slice thickness of 20 mm. CRISTINA phase cycles were chosen identical to option III based on the simulation results for acquisition of B_0-unbiased TQ signal. The multi-echo readout included 20 TEs, with $TE_1 = 1.15$ ms (asymmetric echo) and $\Delta TE = 3$ ms. The TR was 390 ms due to SAR restrictions, and acquisition time was 25 minutes (phantom) and 29 minutes (in vivo) per cycle, which corresponds to 50 minutes and 58 minutes total acquisition time, respectively. The optimal evolution time τ_1 was determined experimentally from a TQTPPI global spectroscopic prescan (scan time 1-2 minutes) and a subsequent offline fit. Thus, employed τ_1 values were: 10 ms in the first phantom (no optimization for pure saline water), 13 ms for the second phantom, and 9.2 ± 1.4 ms for in vivo brain.

In the saline water bottle, a 1D strong static magnetic gradient was applied (~10 Hz/1 cm) to induce offresonance artifact. CRISTINA was compared to its counterpart SISTINA with in vivo phase cycles,[22,27] as defined in Table 1. Because SISTINA uses 6-step phase cycles, the number of averages was set to 20 to match CRISTINA total acquisition time.

3.3 | Experimental data analysis

The first 2 echoes from CRISTINA phase data served to map ^{23}Na signal off-resonance (B_0). Combining CRISTINA 2 phase cycles ($\xi_1 = \pi/2$ and $\xi_2 = 0$), a voxel-wise multiparametric fit of ^{23}Na signal parameters was performed, providing maps of T_2^* slow and T_2^* fast using Equations (2) and (3) and including a Direct Current component to account for background noise. The minimum of the multivariable function was approached with GlobalSearch and fmincon solver in Matlab 2019 (MathWorks, Natick, MA). The value of TQC at TE = 0 ms is 0 from theory and was added to the multi-echo data to enhance the fit. The SQC signal at TE = 0 ms was obtained by extrapolation of the fit result, thus enabling an estimate of a 0 TE ^{23}Na signal. The fit function included both T_2^* fast and T_2^* slow compartments. The fit's lower boundary of the T_2^* fast component amplitude was set to 0 to enable the finding of a mono-exponential solution. Thus, both biexponential and mono-exponential solutions could arise.

In the second phantom, the fitted values were evaluated in circular regions of interest centered over each of the 8 phantom tubes independently, avoiding partial volume effect. Tissue ^{23}Na concentration to signal relationship was evaluated in the region of interest for the SQC image at TE = 0 ms. TQC image at TE = τ_1, normalized by SQC image at TE = 0 ms, was plotted against agar percentage and provided TQ/SQ ratio.

Finally, the SNR was evaluated for phantom and in vivo data on the separated SQ and TQ images over TE. Average signal was measured within the 6-pixel eroded body mask, and noise was evaluated in the complement image of an equivalently dilated body mask to avoid edges.

4 | RESULTS

4.1 | Simulation

The simulation of the original 6-steps phase cycle with neither B_0 inhomogeneity, Ω, nor relaxation effects, option I, is presented as Supporting Information Figure S1 for completeness. The choices for the 6 samples appear relevant to measure the full amplitude of the TQC signal, whereas DQC is not optimally sampled. Also, the choice for 6 samples places the TQC signal at the Nyquist limit. Fourier Transformation along the evolution phase ϕ_1 recovers the amplitudes of the mixed signal of (SQ, DQ, TQ) = (1.0, 0.5, 0.3). The amplitudes in the spectrum do not have a Lorentzian shape because the phase cycle does not capture relaxation processes.

Second, regardless of the time increments (ie, the name TQ(T)PPI), the TQPPI samplings for the 2 phase-cycles with $\xi\backslash, = \pm\pi/2$ are depicted in Figure 2 (see option II). It is demonstrated that the phase increment choice of 45° oversamples the TQC signal. Specifically, the 45° phase increment samples the maximum of the TQC signal only in 2 out of 8 points, with 4 points falling short of measuring the maximum point. In contrast, the sampling points measure optimally the maximum amplitude of the DQC signal, which is opposite in signal for the 2 cycles and hence cancels out when the signals

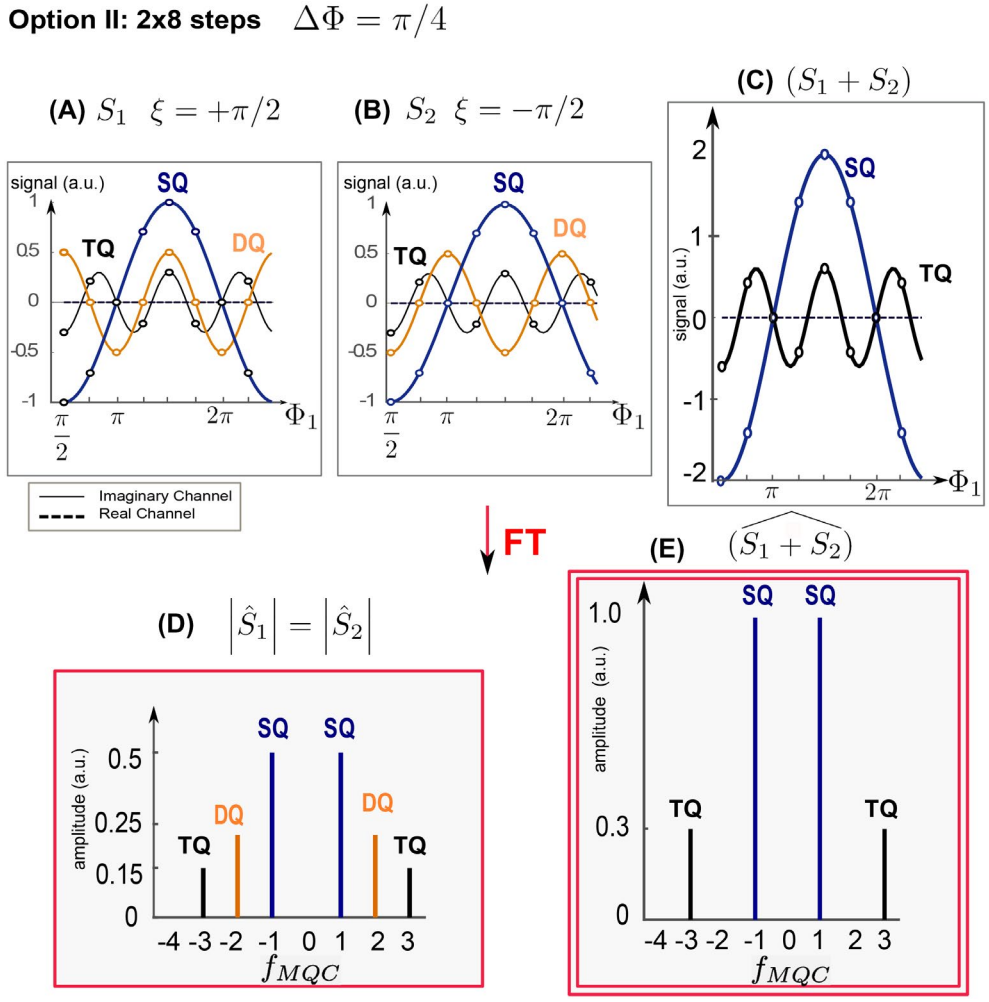

FIGURE 2 Option II: TQ(T)PPI phase cycling. The SQC and DQC are optimally sampled; however, the TQC maximum is only sampled at 2 out of 8 points. Evolution time increment and relaxation have been discarded. The sum of the 2 cycles signals effectively cancels out DQC signal. In the resulting spectra, the DQC cancellation can be observed by FT of the beforehand added signals, and oversampling leads to TQC being split in 2 components. FT, Fourier transform; SQC, single-quantum coherences; TQ(T)PPI, triple-quantum (time) proportional phase increments

are combined. Without considering B_0 offset, the SQC and TQC signal is equivalent for the 2 cycles, with the signal ending up only in the imaginary channel. When relaxation processes and B_0 offsets (100 Hz range) are included (Figure 3), an oscillatory pattern for all quantum coherences was observed with occurrences of complete signal loss. Signal cancellation can be observed for the 2 phase-cycle signals S_1, S_2, and the reconstructed spectra $\hat{S}$ at the same frequency offset (25 Hz and 75 Hz). The signal dropouts can be obtained from Equation (1) for $\Omega = (k\pi + \pi/2)/2\pi\,\tau_1 = (2k + 1)/4\,\tau_1$, $k \in \mathbb{Z}$, which corresponds to the measured dropout values. Further, it can be observed that the DQC signal suppression is also achieved when relaxation processes are considered and a B_0 offset alters the signal. Whereas the MQC magnitude signal is equivalent for the 2 cycles, the phase images show opposite signs for the DQC signal.

The third phase cycling, option III, dubbed here *Fleysher's*,[21] recognized the dramatic signal loss due to B_0 inhomogeneity. The benefit of Fleysher's 2 cycles along with its reconstruction is explained in Figure 4, option III, for an exemplary offset of 10 Hz. The full recovery of the signal (neglecting relaxation) can be seen directly in the amplitude values of the spectrum $\hat{S}_{reco}$.

The full simulation, including relaxation and a range of 100 Hz offsets, shows again an oscillatory pattern for the MQC signals along the B_0 offset, with occurrences of complete signal loss (Figure 5). The key point is that the 2 cycles are complementary in exhibiting signal cancellation and signal maximum. The signal dropouts of the second cycle, $\xi = 0$, are obtained for $\Omega = (k\,\pi + 0)/2\pi\,\tau_1 = k/2\tau_1$. For our set of simulation parameters for example at an offset of $\Omega = \pm 25$ Hz, the signal is recovered in the second phase cycle while being completely canceled in the original phase cycle. The oscillation of the original signal thus has a counterpart in the additional phase cycle.

The simulation results, including STE mitigation, can be found in Supporting Information Figure S1. The STE signal can overlap with MQC signals and shows a relative

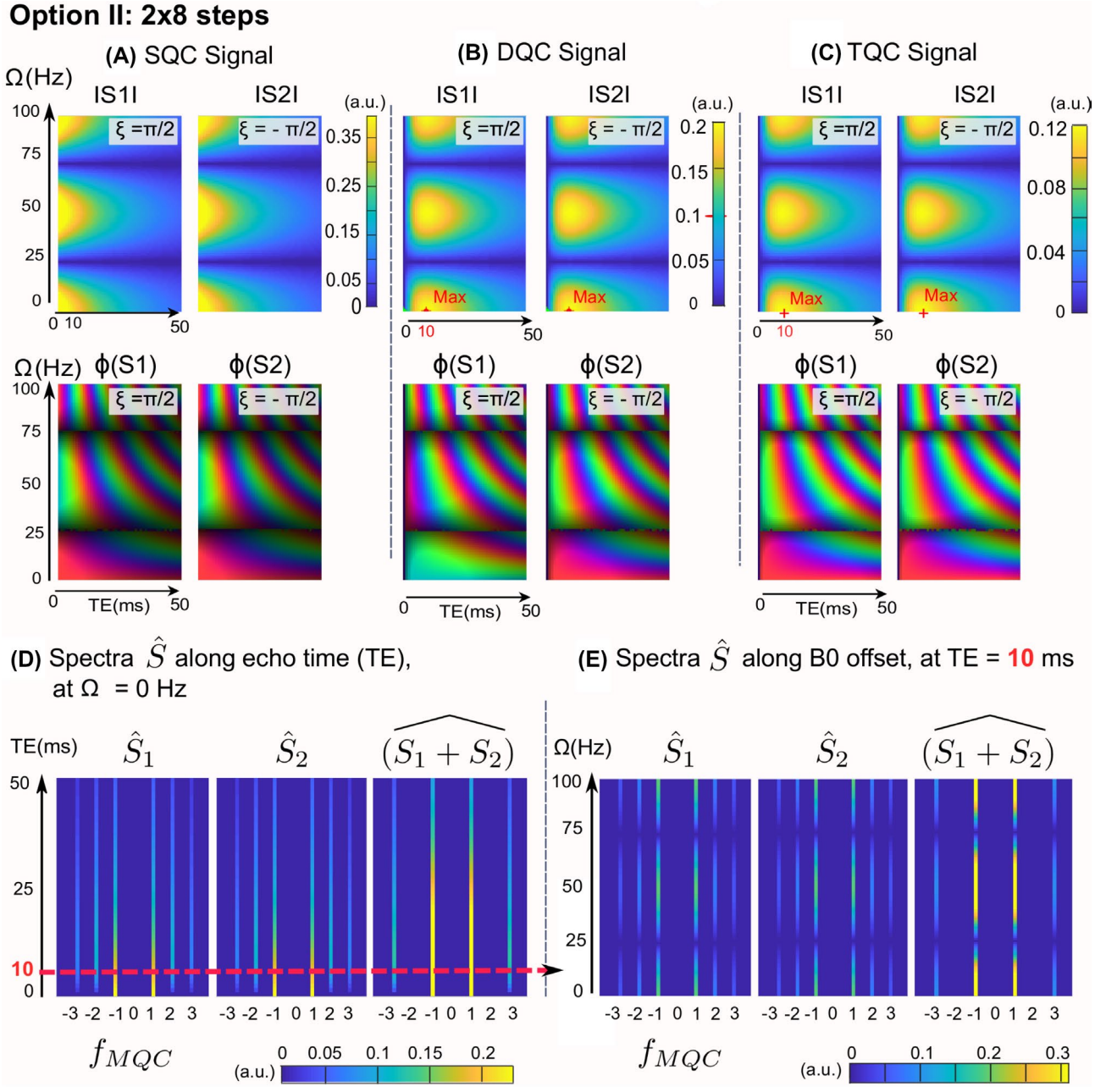

FIGURE 3 Option II: TQ(T)PPI simulation including relaxation and B_0 offset. The magnitude and phase of the signals at ϕ_0 are shown independently for the 3 quantum coherences: (A) SQC, (B) DQC, and (C) TQC. The complex DQC signal (row II) shows signal cancellation due to opposite phases for the 2 phase-cycles. For the SQC and TQC signals, signal addition is constructive. (D,E) The spectra for the individual phase cycles ($\xi = \pm \pi/2$), as well as for the added signals in (D) along the B0 offset and (E) along the TE. Signal cancellation at 25 and 75 Hz can be observed

maximum signal at an TE equal $\tau_1 = 10$ ms, which coincides with the maximum signal of the TQC signal (Figure 5). The STE phase signal is the opposite for phase cycles proposed by SISTINA; thus, the sum of the complex STE signals of the 2 cycles cancels out.

However, considering STE signal expression, one can observe that STE is independent of the phase increment ϕ_1 because its phase term is $\exp\left(i\left(p_1\phi_1 + (0-p_1)\phi_2\right)\right) = \exp\left(ip_1\xi\right)$. Thus, STE signal can be considered as a zero-quantum coherence signal (Supporting Information Figure S2). Finally, inserting measured B_0 offset into Equation (5) of the STE signal can nullify STE signal within the reconstruction. The alternatively proposed sum-of-squares magnitude reconstruction, as indicated in the SISTINA publication,[22] still showed the STE signal as an offset.

Figure 6 compares the complete signal recovery from 2 cycles, as defined in Fleysher and presently, to the signal from the 4 cycles defined in SISTINA (see Table 1). B_0-induced signal nulling in $\hat{S}_1$ and $\hat{S}_2$ was compensated for using paired cycles $\hat{S}_3$ and $\hat{S}_4$, as shown in the reconstructed combination

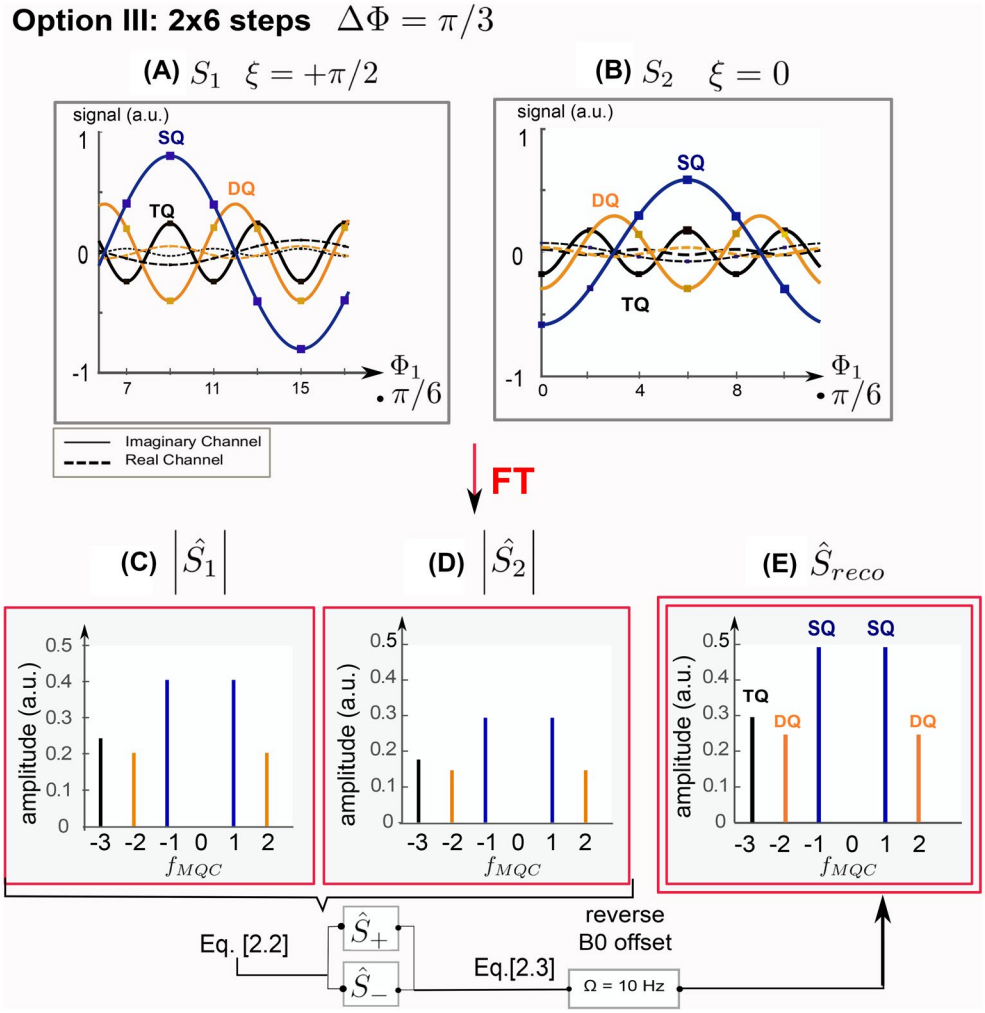

FIGURE 4 Option III: Fleysher cycles for recovering B_0 offset bias of 10 Hz. (A), (B) show the signal, S_1 and S_2, along the phase cycle for $\xi = \pi/2$, 0.(C) and (D) show the individual Fourier transformed amplitudes highlighting that some signal ended up in the S_2. Their addition and subtraction $\hat{S}_{\pm}$, in combination with a reverse of the known B_0 offset, result in the recovered spectrum (E). The amplitudes in (E) are the initially set values for the simulation, which shows that the signal was effectively recovered, reversing the B_0 offset effect

$\hat{S}_1+\hat{S}_3$ (Figure 6B). However, SISTINA choice to prefer the first cycles S_1 and S_2 for all in vivo experiments remains sensitive to B_0-induced signal loss.

In summary, it appears crucial to compensate for B_0 offsets, whereas STE is inherently isolated upon Fourier transform of the MQC signals, as is DQC. Thus, an efficient choice for MQC measurements is Fleysher's 2 × 6-steps phase cycles. But SISTINA's design offered an interesting addition by electing for a multi-TEs readout to sample MQC signals along time (alas, in a larger raster time than TQ(T) PPI). Therefore, the combined design of 2 × 6-steps phase cycles and a multi-echo CRISTINA was implemented and investigated on phantoms and in vivo in the following.

4.2 | Experimental measurements

Experimental comparison of CRISTINA and SISTINA shown in Figure 6C confirms SISTINA sensitivity to B_0 when using only the 2 in vivo cycles, whereas CRISTINA design allows for a B^0-resilient reconstruction of SQC signal (and by extension TQC). The signal loss between CRISTINA and SISTINA oscillates between 20% and 50% due to intravoxel signal averaging within large acquired voxels.

Figure 7 shows experimental design, including the CRISTINA sequence diagram (A), raw images (B), and the postprocessing results (C) exemplary from 1 voxel as well as for the whole image. The estimated τ_1 from a TQTPPI global spectroscopic prescan (scan time ~30 seconds) was 13.3 ms. Two series of 4D images were obtained with the dimensions being x, y, TE, and ϕ_1. The Fourier transform along the repeated (10×) phase cycle dimension ϕ_1 over the complex signal images showed the MQC spectrum as anticipated from the simulations. Selecting single and triple quantum coherence frequencies, the SQ and TQ images were reconstructed. Subsequently, $\hat{S}_+$ and $\hat{S}_-$ were calculated. A B_0 map was also computed using the phase difference (unwrapped) between the first 2 TE after quadrature combination of the 2 phase-cycles

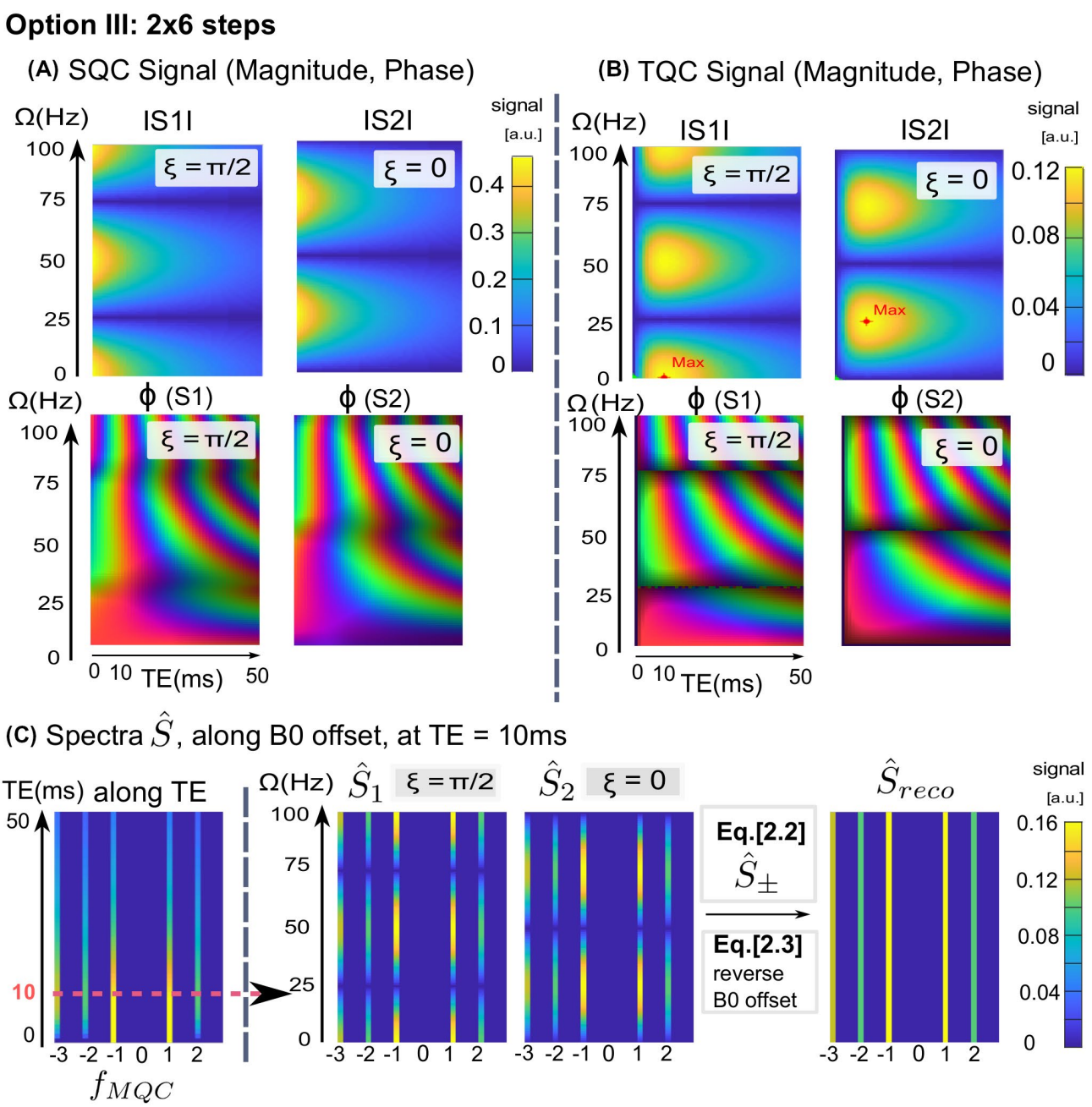

FIGURE 5 Option III: Fleysher cycles, along TE (0 ms–50 ms) and varying B_0 offset from 0 Hz up to 100 Hz. Magnitude and phase signal are shown for the SQC (A) and TQC (B) to show the differing oscillation due to B_0 offset. This offers the possibility of signal reconstruction, shown in the spectra data in (C). Signal evolution with differing signal maxima of SQC and TQC signal along TE is given for no B_0 offset. Then the spectra are given at TE = 10 ms along a B_0 offset from 0 to 100 Hz. Signal vanishing can be observed at 25 and 75 Hz offset in the first cycle and at 0, 50, and 100 Hz in the second cycle. The reconstructed spectrum is independent of the B_0 field offset. CRISTINA makes use of the same 2 phase cycles

and averaging over phase cycle steps. Eventually, total SQC and TQC signal images were reconstructed for each TE. Data and processing results for a single voxel can be found in the Supporting Information Figure S3, with the intention to enhance comparability to the simulation results.

A subsequent multiparametric fit for the SQC and TQC signals (Equations (2) and (3)) was performed voxel-wise along the TE data, enhanced by the prior knowledge that TQC is 0 at TE = 0 ms. The results are presented in Figure 8. The SQC signal evolution fit over the multiple TEs allowed for extrapolation of the SQC signal to TE = 0 ms. The TQC signal image is shown for TE = τ_1 = 13.3 ms. Exemplary, the signal evolution measurement data with the corresponding fit results are shown for the 8 center voxels of the phantom vials along TE, in range of 0 to 60 ms, separately for the SQC and TQC signal (Figure 8H,I). The characteristic signal evolution of SQC and

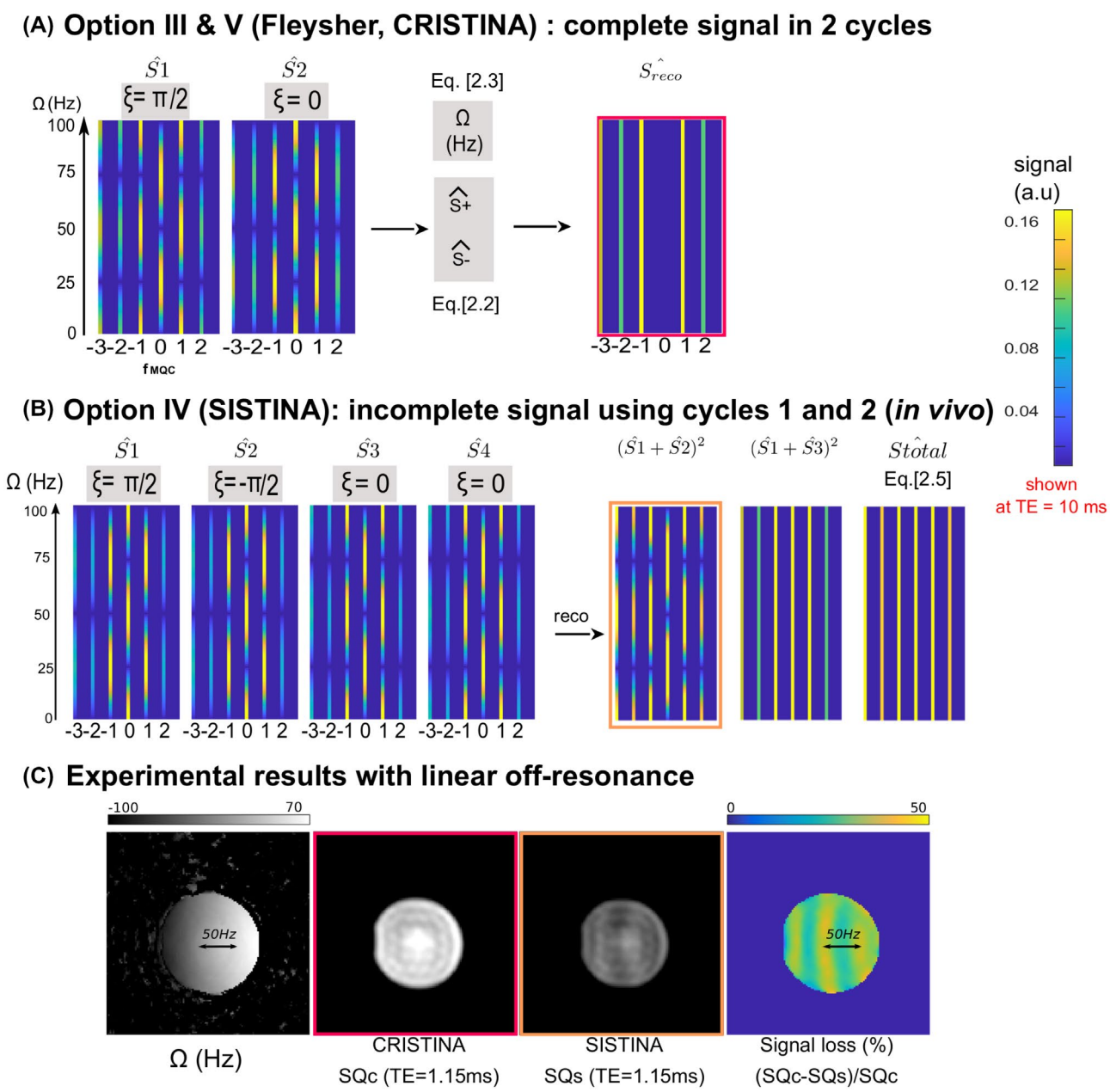

FIGURE 6 A, Option III and V phase cycle recovers signal from B_0-induced signal loss using only 2 cycles. B, Option IV assumed 4 cycles necessary to recover the signal, and most importantly, prioritized the first 2 cycles for all in vivo experiments. This combination led to remaining B_0-induced signal loss. C, Experimental results from a homogeneous phantom with induced strong B_0 gradient. Images are scaled identically. Excellent signal recovery is demonstrated from CRISTINA (option V), whereas SISTINA (option IV) shows dark bands spaced regularly by $1/(2\tau_1) = 50$ Hz in this case. Signal loss ranges from 20% to 50% due to partial volume effect from large voxel size

TQC signals from the simulation was confirmed. Eventually, T_2^* fast and T_2^* slow maps were produced from the multiparameter fit with values in the range of 0 to 12 ms for T_2^* fast and 15 to 30 ms for T_2^* slow. The liquid phantom vial followed essentially a monoexponential decay for most pixels. The 2% agar vial in the center showed elevated T_2^* fast values in the range of (11.0 ± 2.7 ms) and lower T_2^* long values of (21.9 ± 3.1 ms) compared to the 4% and 5% agar phantoms with T_2^* fast in the order of 5 ms and T_2^* long in the order of 27 ms.

Further, mean SQC signal evaluated in region of interest at TE = 0 ms showed a linear relationship against total ^{23}Na content in mM ($R^2 = 0.75$, P value = .0058). For the mean TQC signal, normalized by SQC at TE = 0 ms, a higher signal strength was observed for increased agar content, regardless of the ^{23}Na concentration ($R^2 = 0.87$, P value = 0.0007). However, for the 4% and 5% agar content, the mean TQC/SQC difference was within the ROI SDs.

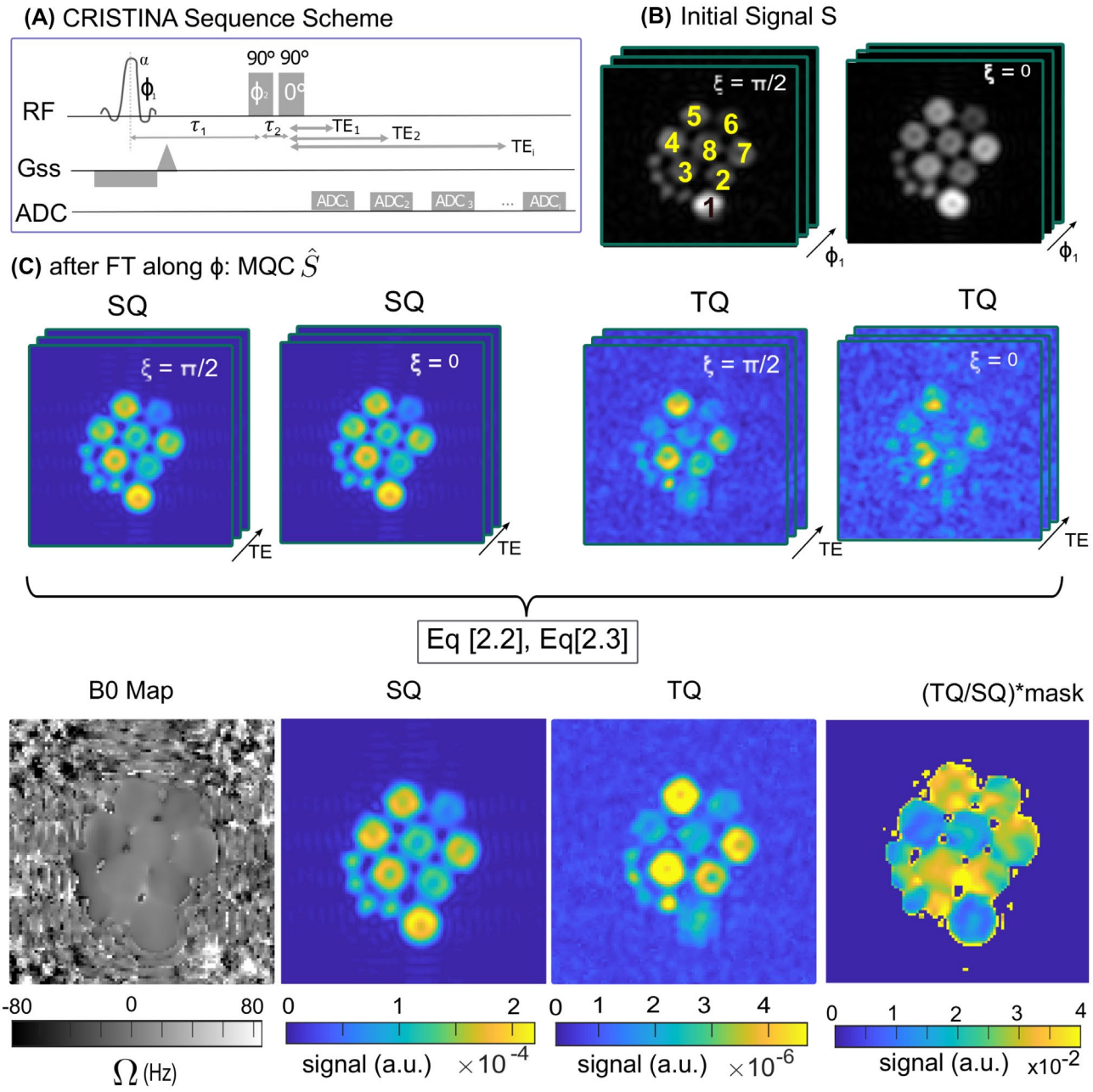

FIGURE 7 A, 2D multi-echo sequence scheme B, initial phase cycle signal image at $\Phi_{1,t=0}$ D, from the phase cycle data; the spectroscopic images were reconstructed by voxelwise FT for each TE set. $\hat{S}_{\pm}$ were calculated. The B_0 map was calculated from quadrature combination of the 2 cycles and the multi-TE experiment. Using the voxelwise B_0 offset values, the total spectroscopic result, $\hat{S}_{total}$, was reconstructed. A complex signal depiction of a voxel of interest in phantom 5 can be found in Supporting Information Figure S3

Feasibility of in vivo CRISTINA is demonstrated in Figure 9. CRISTINA shows excellent resilience to B_0 inhomogeneity, such as in the first volunteer in which B_0-shimming was not iterated. SQ images at TE = 1.15 ms exhibit expected ^{23}Na distribution in the brain despite significant partial volume effect of cerebrospinal fluid due the thick prescribed 2D slice (20 mm).

SQ images SNR were comparable between phantom and in vivo data (76 ± 27 vs. 80 ± 11, respectively, for the first TE). However, TQ SNR in vivo was much lower compared to phantom (14 ± 7 vs. 5 ± 0.5 at TE = 10 ms). Therefore, voxelwise signal fitting was not deemed reliable in vivo (Supporting Information Figures S4 and S5).

5 | DISCUSSION

In this study, the rationales for the various sequence designs for MQC ^{23}Na-MRI measurement were considered in a unified formalism, theoretically and graphically. From

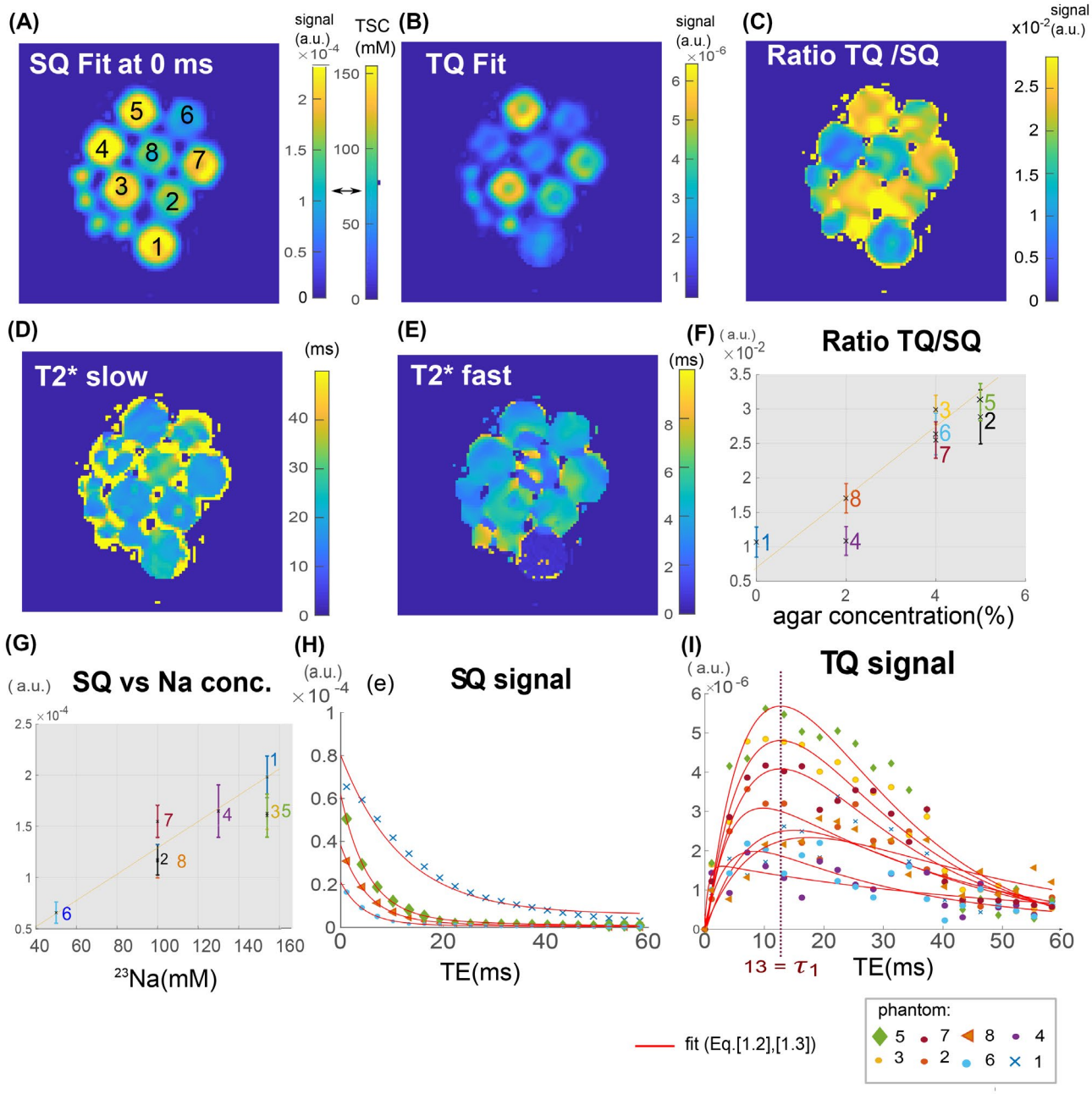

FIGURE 8 A, Fitted SQ signal, extrapolated to TE = 0 ms. The colorbars show the signal strength and the sodium concentration in mM by a linear fit using the (2%, 130 and 100 mM) phantoms for calibration. Phantoms are numbered for the following: B, TQ signal at TE 13.3 ms with higher signal strength in phantoms 3 and 5 (4%, 5% agar, 154 mM). C, TQ to SQ ratio relates to agar values, independent of ^{23}Na content. D, E, T_2^* slow and T_2^* fast maps by voxelwise fit. The liquid phantom 1 showed a monoexponential result and therefore has values close to 0. F, TQ to SQ ratio is visualized against agar concentration and showed a linear relationship ($R^2 = 0.87$). G SQ signal at TE = 0 ms showed a linear relationship to ^{23}Na concentration ($R^2 = 0.75$). Values in (F,G) were evaluated and averaged over the tube size. H, SQ signal over TE and fit, only 4 phantoms, different in agar and sodium concentration, are depicted to ease visual comparison. I, TQ signal over TE time and fit. T_2^* slow and T_2^* fast values, along with the concentrations of each of the numbered phantoms, can be found in the Supporting Information Table S1 and summarizes all resulting values

the improved understanding of the different options, an efficient design was proposed to compensate for B_0 and stimulated echo in only 2 × 6-steps phase cycles. The proposed CRISTINA sequence further leveraged multi-echo readout to rapidly sample MQC signal temporal evolution. Eventually, CRISTINA data were enhanced by the unified formalism to draw a complete characterization of the ^{23}Na signal, including B_0, relaxometry, and total signal of both SQC and TQC.

Although different options have been presented over the last decades, an overview and comparison between the various techniques was lacking. Furthermore, we presented a

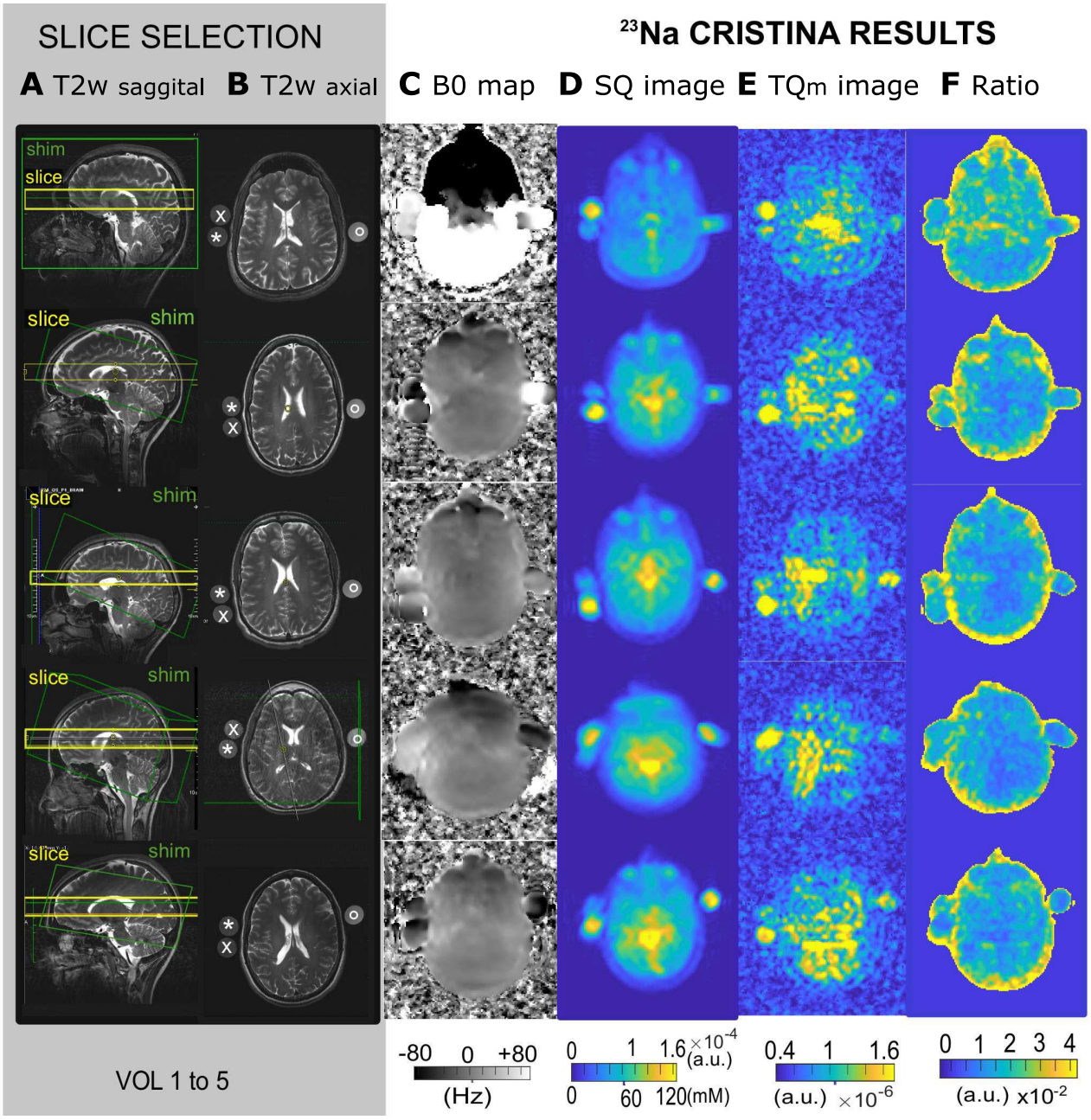

FIGURE 9 A, B, T_2w image and the 2D slice position for the sodium acquisition in coronal and axial view. Phantoms are indicated with (x, *, o) for (100 mM and 4% agar, 50 mM and 4% agar, 100 mM and 2% agar). C, initial phase cycle signal at $\Phi_{1,t=0}$ for the first cycle D, reconstructed SQ image for the first cycle. E, F, TQ images for both cycles. G, B_0 map leading to the total spectroscopic signal, $\hat{S}_{total}$. To enhance SNR, the TQ images are averaged from the 2nd to the 7th echo, which equals the TEs from 4 to 18 ms

graphical and intuitive formalism to simulate the techniques of coherence transfer and phase cycling, with publicly available code for reproducibility.

The understanding of the different options for measuring TQC signal, along with the resulting efficient phase-cycling choice, are especially important because ^{23}Na MR techniques are on the rise thanks to hardware improvements. Eventually, probing MQC signal in ^{23}Na MRI allows full capture of the underlying physical properties within each voxel. Indeed, as shown in Figure 8, both T_2^* compartments relaxation properties and total ^{23}Na concentrations can be inferred provided that a calibrated sample is within the imaging plane. Thus, the pairing of the common theoretical framework presented above with the experimental design for efficient MQC ^{23}Na MRI can provide refined tissue characterization and hence diagnostics and treatment monitoring.

Simulation results showed that the conventional 6-step phase cycle is, expectedly, most susceptible to B_0

inhomogeneity. The additional phase cycle with a phaseshift of 0° for B_0 inhomogeneity mitigation effectively alleviates the problem.

The TQTPPI method proposed a different second phase cycle to suppress DQC signals. However, the DQC signal is differentiated by Fourier decomposition and ends up at twice the single quantum coherence frequency, whereas the TQC signal ends up at 3 times the SQC frequency. Therefore, the additional cycle for DQC transfer suppression doubles the measurement time with merely an averaging repetition of the SQC and TQC signal. The 45° ($2\pi/8$) phase increment oversamples TQC and misses capture of the full TQC signal amplitude. The Nyquist sampling frequency is twice the highest frequency of interest, resulting in a maximum phase increment of 60° for efficient TQC sampling. Any smaller phase increment results in oversampling and serves to accumulate signal, which can be substituted by averaging. The advantage of the TQTPPI method using time proportional phase increments is given in the possibility of obtaining the T_2^* long and short values from the fit of the signal along the evolution time without prior knowledge of the optimal evolution time. A standard phase-cycle with fixed evolution time τ_1 and 1 single echo readout in an imaging experiment cannot provide this information. The Fleysher's 2-phase cycles choice focused on the B_0 offset mitigation. This design effectively helps resolve any lost signal and remove STE and DQC signals impact while operating at the Nyquist frequency.

The SISTINA design focused on 4 phase cycles to suppress stimulated echo signals. Although the stimulated echo signal is the highest at the time point of the maximum TQC signal, the stimulated echo signal assimilates to a zero-quantum coherence signal, that is, as a continuous offset, after Fourier decomposition. SISTINA's interesting aspect was the multiple echo readout that allows capture of the temporal evolution of both SQC and TQC. A further addition of the SISTINA sequence[22,27] was the use of the "dead" time between the first and the second pulse for 1 or multiple UTE readouts. These additional measurements can serve to improve the overall SNR; however, combining UTE and further Cartesian images with proper signal scaling is nontrivial. Our CRISTINA results also demonstrate complete SQC signal characterization without UTE sampling.

Eventually, CRISTINA added values over SISTINA are multiple and arise from the proposed theoretical framework that was incomplete in the SISTINA design[28]:

First, SISTINA considered 4 cycles to be necessary to complete ^{23}Na signal characterization. As demonstrated in Figure 6, CRISTINA 2 cycles suffice to compensate B_0-induced signal loss and phase cycling inherently separates STE from MQC signals. Thus, in vivo SISTINA results have been limited to B_0 homogeneity under $(2k + 1)/(4 \times 7\text{ ms}) = \pm 35$ Hz[27] and $(2k + 1)/(4\times 6\text{ ms}) = \pm 42$ Hz,[22] with $k \in \mathbb{Z}$. Second, CRISTINA relies only on Cartesian sampling, whereas SISTINA is based on a joint model including half-radial UTE signal sampling and Cartesian sampling. UTE sampling is dedicated to measure rapidly decaying signal but suffers from accrued sensitivity to hardware imperfections[29] that usually require platform-depend tuning and corrections. Utilizing Cartesian sampling may facilitate reproducibility across platforms and avoid the issue of scaling UTE and MQC Cartesian signals to jointly model signal relaxation.

Finally, CRISTINA additionally provides a B_0 map that can serve the model from Equation (8). If B_0 values were unavailable, a quadrature combination of the 2 cycle can be substituted, alas without exact signal phase.

Thus, an efficient MQC ^{23}Na-MRI sequence design named *CRISTINA* was drawn that benefits from the efficient Fleysher's 2 × 6-steps phase cycles, in combination with SISTINA multi-echo readout to mimic TQTPPI assumption-free signal sampling. CRISTINA leads to a complete characterization of ^{23}Na signal, including B_0, relaxation times, and MQC signals.

5.1 | Experimental proof of concept

CRISTINA design was empowered by the theoretical formalism to extract MQC signals free of B_0, DQC, and STE biases. The reconstruction of the acquired Cartesian MQC data can be done straightforwardly using Fourier transform. B_0 can be mapped using a simple least-square fit of the phase data. A multiparametric fit results in T_2^* fast and T_2^* slow maps as well as quantification values for SQC and TQC signals. The asymmetric echo choice reduced the lowest possible TE to 1.15 ms. With extrapolation of the fit, a TE = 0 ms SQC image can be reconstructed, which allows total ^{23}Na content quantification without bias due to differing decay rates. Therefore, all relevant information for quantification methods can be obtained with the sequence.

Further optimization remains to be considered regarding acquisition parameters such as TE sampling and receiver bandwidth. Currently, the phantom measurement took 25 min per phase cycle but was chosen with conservative values of twofold oversampling the TQ frequency by $\Delta\phi = 30°$ and measurement of 10 full phase cycles for averaging. The total measurement time of 50 min could, therefore, be reduced by $\Delta\phi = 60°$ and fewer phase cycles. The matrix size of 48 × 32 was chosen, and the higher resolution was achieved by zero filling. Individual phantom vials could potentially suffer from a partial volume effect due to the 2D acquisition with chosen slice thickness of 20 mm and imperfect parallel alignment of the vials; additionally, high agar concentrations can lead to an inhomogeneous gel distribution, and both can explain deviations between similar vials.

In vivo measurements were successfully conducted with the same parameters. Twelve full cycles were acquired,

which resulted in an acquisition time of 29 minutes per cycle. Further tests in vivo are necessary to reduce the measurement time and for higher resolution scans without sacrificing SNR in the TQ image. Postprocessing of the cycle repetitions and the multiparametric fit could be optimized in the future by, for example, using a neural network approach[30,31] and even considering the multiple dimensions instead of working voxel per voxel. Moreover, it must be noted that, at present, CRISTINA remains a 2D imaging sequence, and for the presented measurement set a relatively thick slice of 20 mm was used. To overcome partial volume effects, the presented CRISTINA will be extended to 3D measurement in the next step. (Phantom measurement raw data and reconstruction code can be found here: https://github.com/MHoesl/MQC_Imaging_CRISTINA).

6 | CONCLUSION

We presented a full simulation analysis of the different possible phase cycles for ^{23}Na multi-quantum MRI and highlighted their benefits and shortcomings. An efficient sequence design was drawn, resulting from the simulation work, and implemented on a clinical MRI. An experimental proof of concept on a phantom shows promising results for a complete characterization of the multiquantum ^{23}Na signals.

ACKNOWLEDGMENT

This article is based in parts upon work from COST Action "CA16103 Assessment of Kidney Physiology using 23Na triple quantum spectroscopy," supported by COST (European Cooperation in Science and Technology). This work was performed by a laboratory member of France Life Imaging network (grant ANR-11-INBS-0006). This work was performed on the platform 7 T-AMI, a French "Investissements d'Avenir" programme" (grant ANR-11-EQPX-0001).

ORCID

Michaela A. U. Hoesl https://orcid.org/0000-0002-9177-1470
Stanislas Rapacchi https://orcid.org/0000-0002-8925-495X

REFERENCES

1. Jaccard G, Wimperis S, Bodenhausen G. Multiple-quantum NMR spectroscopy of S=3/2 spins in isotropic phase: a new probe for multiexponential relaxation. *J Chem Phys*. 1986;85:6282.
2. Bodenhausen G, Kogler H, Ernst RR. Selection of coherence-transfer pathways in NMR pulse experiments. *J Magn Reson*. 1984;58:370-388.
3. Bodenhausen G, Vold RL, Vold RR. Multiple quantum spin-echo spectroscopy. *J Magn Reson*. 1980;37:93-106.
4. Pekar J, Leigh JS. Detection of biexponential relaxation in sodium-23 facilitated by double-quantum filtering. *J Magn Reson*. 1986;69:582-584.
5. van der Maarel JRC. Relaxation of spin quantum number S=3/2 under multiple-pulse quadrupolar echoes. *J Chem Phys*. 1991;94:4765.
6. Romanzetti S, Mirkes CC, Fiege DP, Celik A, Felder J, Shah NJ. Mapping tissue sodium concentration in the human brain: a comparison of MR sequences at 9.4 Tesla. *Neuroimage*. 2014;96:44-53.
7. Thulborn KR. Quantitative sodium MR imaging: a review of its evolving role in medicine. *Neuroimage*. 2018;168:250-268.
8. Wagner D, Anton M, Vorwerk H. Dose uncertainty in radiotherapy of patients with head and neck cancer measured by in vivo ESR/alanine dosimetry using a mouthpiece. *Phys Med Biol*. 2011;56:1373-1383.
9. Hu R, Kleimaier D, Malzacher M, Hoesl MAU, Paschke NK, Schad LR. X-nuclei imaging: current state, technical challenges, and future directions. *J Magn Reson Imaging*. 2020;51:355-376.
10. Hoesl MAU, Kleimaier D, Hu R, et al. ^{23}Na Triple-quantum signal of in vitro human liver cells, liposomes, and nanoparticles: cell viability assessment vs. separation of intra- and extracellular signal. *J Magn Reson Imaging*. 2019;50:435-444.
11. Van Der Maarel JRC. Thermal relaxation and coherence dynamics of spin 3/2. I. Static and fluctuating quadrupolar interactions in the multipole basis. *Concepts Magn Reson*. 2003;19A:97-116.
12. Van Der Maarel JRC. Thermal relaxation and coherence dynamics of spin 3/2. II. Strong radio-frequency field. *Concepts Magn Reson*. 2003;19A:117-133.
13. Tanase C, Boada FE. Triple-quantum-filtered imaging of sodium in presence of B0 inhomogeneities. *J Magn Reson*. 2005;174:270-278.
14. Schepkin VD. Statistical tensor analysis of the MQ MR signals generated by weak quadrupole interactions. *Z Med Phys*. 2019;29:326-336.
15. Levitt MH. *Spin Dynamics: Basics of Nuclear Magnetic Resonance*. 2nd ed. Chichester: John Wiley & Sons; 2000.
16. Rooney WD, Springer CS. The molecular environment of intracellular sodium: ^{23}Na NMR relaxation. *NMR Biomed*. 1991;4:227-245.
17. Kemp-Harper R, Brown SP, Hughes CE, Styles P, Wimperis S. ^{23}Na NMR methods for selective observation of sodium ions in ordered environments. *Prog Nucl Magn Reson Spectrosc*. 1997;30:157.
18. Navon G, Shinar H, Eliav U, Seo Y. Multiquantum filters and order in tissues. *NMR Biomed*. 2001;14:112-132.
19. Rance M, Sørensen OW, Bodenhausen G, Wagner G, Ernst RR, Wüthrich K. Improved spectral resolution in COSY 1H NMR spectra of proteins via double quantum filtering. *Biochem Biophys Res Commun*. 1983;117:479-485.
20. Schepkin VD, Neubauer A, Nagel AM, Budinger TF. Comparison of potassium and sodium binding in vivo and in agarose samples using TQTPPI pulse sequence. *J Magn Reson*. 2017;277:162-168.
21. Fleysher L, Oesingmann N, Inglese M. B0 inhomogeneity-insensitive triple-quantum-filtered sodium imaging using a 12-step phase-cycling scheme. *NMR Biomed*. 2010;23:1191-1198.
22. Fiege DP, Romanzetti S, Mirkes CC, Brenner D, Shah NJ. Simultaneous single-quantum and triple-quantum-filtered MRI of ^{23}Na (SISTINA). *Magn Reson Med*. 2013;69:1691-1696.
23. Burstein D. Stimulated echoes: description, applications, practical hints. *Concepts Magn Reson*. 1996;8:269-278.

24. Hahn EL. Spin echoes. *Phys Rev*. 1948;73:580-591.
25. Kingsley PB. Product operators, coherence pathways, and phase cycling. Part II. coherence pathways in multipulse sequences: spin echoes, stimulated echoes, and multiple quantum coherences. *Concepts Magn Reson*. 1995;7:115-136.
26. Matthies C, Nagel AM, Schad LR, Bachert P. Reduction of B0 inhomogeneity effects in triple-quantum-filtered sodium imaging. *J Magn Reson*. 2010;202:239-244.
27. Worthoff WA, Shymanskaya A, Shah NJ. Relaxometry and quantification in simultaneously acquired single and triple quantum filtered sodium MRI. *Magn Reson Med*. 2019;81:303-315.
28. Burstein D, Springer CS Jr. Sodium MRI revisited. *Magn Reson Med*. 2019;82:521-524.
29. Tyler DJ, Robson MD, Henkelman RM, Young IR, Bydder GM. Magnetic resonance imaging with ultrashort TE (UTE) PULSE sequences: technical considerations. *J Magn Reson Imaging*. 2007;25:279-289.
30. Schnurr AK, Chung K, Russ T, Schad LR, Zöllner FG. Simulation-based deep artifact correction with Convolutional Neural Networks for limited angle artifacts. *Z Med Phys*. 2019;29:150-161.
31. Lundervold A. Analysis of texture: practice. In Proceedings of the International Society for Magnetic Resonance in Medicine, Montréal, Québec, Canada, 2011. pp. 19-20.

SUPPORTING INFORMATION

Additional Supporting Information may be found online in the Supporting Information section.

TABLE S1 Mean phantom T_2^* values, evaluated in a circular ROI of phantom diameter size. The four smaller diameter phantoms were not taken into account and served to see if smaller structures can be resolved

FIGURE S1 Option I: Original six step phase cycle: A, The three coherence signals contributions over the evolution phase ϕ_1 dimension. Circle markers highlight sampling values for phase increment of $2\pi/6$ and start phase of $\pi/6$. B, Fourier Transform splits the MQC contributions and thus allows to separate the three contributions SQ, DQ and TQ, with TQ signal at the Nyquist horizon

FIGURE S2 Stimulated echo signal (STE) arises from the 3-pulses scheme and occurs at TE= τ_1. STE signal can overlap with MQC signals, which can be seen in (A) and shows a relative maximum signal of 0.16 (red cross) at an echo time of TE= $\tau_1 = 10$ ms which coincides with the maximum signal of the TQC signal However, filtering for MQC signals imposes RF phase cycling that isolates STE as a zero-quantum (ZQC) signal. Beyond isolating STE signal using phase cycling, inserting off-resonance values into Equation (5) allows the reconstruction to completely null STE signal

FIGURE S3 For better comparison to the simulation data, a single voxel of interest within Phantom 5, 154 mM Na, 5% agar is presented. A,B, image data with the voxel of interest marked by a cross. C, Real and Imaginary parts of the two cycles are plotted along ϕ_1 with the circular markers indicating data acquisition. D,E, spectroscopic result along the multiple echo times. (D) TQ signal can be seen well (E) no visible TQ signal in (E). F, The data are reconstructed to a total spectroscopic result free of B0 inhomogeneity bias

FIGURE S4 Signal to noise ratio (SNR) over echo time, TE. A, SNR was calculated as the mean signal in the foreground divided by the standard deviation of the background noise region. Foreground region was defined using an eroded bodymask after manual thresholding. Background region was defined using the complementary mask after dilation to exclude measurements from boundary signal. Reported in vivo SNR has been averaged over the 5 healthy volunteers. B, TQ SNR for the individual phantom vials, evaluated in a manually selected circular region that excluding edges

FIGURE S5 An exemplary one voxel fit in the indicated region for each of the 5 volunteers is given. Further development of the fitting routine is necessary to allow the fit in vivo in reasonable time on low SNR images with larger FOV and smaller voxels

How to cite this article: Hoesl MAU, Schad LR, Rapacchi S. Efficient ^{23}Na triple-quantum signal imaging on clinical scanners: Cartesian imaging of single and triple-quantum ^{23}Na (CRISTINA). *Magn Reson Med*. 2020;84:2412–2428. https://doi.org/10.1002/mrm.28284